2020-08

Propeller and vortex ring state for floating offshore wind turbines during surge

Kyle, R

Propeller and vortex ring state for floating offshore wind turbines during surge

Ryan Kyle[a,*], Yeaw Chu Lee, Wolf-Gerrit Früh

[a]School of Engineering and Physical Sciences (EPS), Heriot-Watt University, Edinburgh, EH14 4AS, UK.

Abstract

Surge motion of a floating wind turbine can lead to conditions where the rotor moves backwards faster than the wind, leading to propeller-like conditions or vortex ring state (VRS). The effect of surge on the thrust of a floating turbine was investigated with OpenFOAM for conditions favourable to propeller and vortex ring state. Due to lower blade velocities and larger blade twists, a region of negative thrust is shown to extend spanwise from the blade root towards the tip signifying propeller state. Predictions that strong waves with low/moderate wind speeds leads to propeller-like conditions were confirmed for a representative surging simulation with a 9.4 m amplitude in waves with an 8.1 s period and 7 m/s wind speed. A negative thrust for the entire rotor, through the combination of an inboard region of negative and outboard region of small but still positive thrust, was observed during the expected part of the surging cycle. VRS was observed with blade tip-vortex interaction and root vortex recirculation due to the duration with a negative relative rotor velocity being similar to the blade passing period, inhibiting vortex advection downstream. This work explains and demonstrates the causes of propeller state and VRS for floating turbines.

Keywords: Floating offshore wind turbine, surge motion, propeller state, vortex ring state, CFD, OpenFOAM

1. Introduction

Floating offshore wind turbines promise the ability to harness high-quality wind resource in waters too deep for fixed-base configurations [1]. Although having the potential for a higher energy yield, the additional motions associated with floating platforms presents a new set of challenges as the forces experienced by the rotor become more complex than a fixed-base equivalent [2]. These extra motions create a fluctuation in the relative velocity seen by the rotor which in turn has an impact on its aerodynamics. They are described by six additional degrees of freedom; three translational (surge, sway and heave along the x, y and z axes, respectively) and three rotational (roll, pitch and yaw about the x, y and z axes, respectively), as shown in Fig. 1. At present, there are generally three platform classifications that are used to identify the method of flotation for floating offshore wind turbines: semi-submersible, spar-buoy and tension-leg platform (TLP) types [2, 3, 4, 5]. These platforms are buoyancy, ballast and mooring line stabilised, respectively. Two examples of commercial platforms are the WindFloat buoyancy-type platform by Principle Power [7], and the Hywind ballast-type platform that was deployed on the Hywind demonstrator farm by Equinor [4]. Other commercial platforms up to 2015 are summarised in a report by the Carbon Trust [4].

Whilst most numerical studies of floating offshore wind turbines experiencing motion to date are based on the NREL 5MW wind turbine [8], discussed in more detail in §2, the method of simulation varies. For example, the free-vortex method (FVM), utilising the Biot-Savart equations, was adopted by Wen et al. [9], Shen et al. [10] and Farrugia et al. [11] with surge in isolation. The FVM is a very effective tool when determining the flow field behind a floating turbine, as studied by Sebastian & Lackner [12, 13, 14], but does not fully capture the flow detail during heavily unsteady or separated flows across the rotor blades and is therefore inadequate for highly dynamic cases.
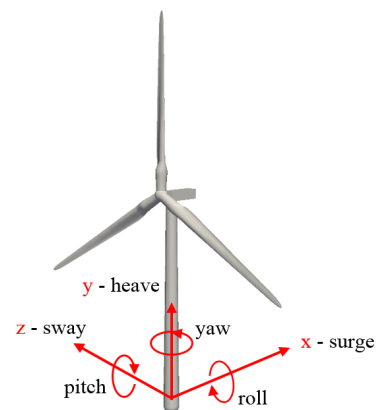
Finite volume CFD solvers, although more computa-

Figure 1: The additional degrees of freedom associated with a floating offshore wind turbine.

*Corresponding author.

Email addresses: rak18@hw.ac.uk (Ryan Kyle), Y.C.Lee@hw.ac.uk (Yeaw Chu Lee), W.G.Früh@hw.ac.uk (Wolf-Gerrit Früh)

tionally expensive, are used to retain flow detail and accuracy during examples of highly unsteady flow. Researchers who have adopted this for floating offshore turbines include Tran et al. [15, 16, 17], Wu et al. [18] and Liu et al. [19]. In those studies, the Reynold's Averaged Navier-Stokes equations are solved using the k-ω SST turbulence model for closure [20]. The choice of mesh movement when using CFD varies as the mesh dynamics for a floating offshore turbine can be intricate. Wu et al. [18] and Liu et al. [19] adopted a sliding mesh technique, where a mesh region surrounding the rotor moves separately from the background domain yet transfers information between the two regions by maintaining physical contact with each other. Tran et al. [15, 16, 17] used an overset-mesh method which creates mesh domains that overlap and move independently from one another. Although the overset technique is slightly more computationally expensive than others [21], it greatly simplifies the dynamic mesh problem for complex or multi-geometry cases.

Over the past decade it has been generally accepted that the motions associated with a floating offshore wind turbine have a significant impact on the rotor aerodynamics, depending on the sea states the platform is exposed to. If the wind turbine is stationary or if it moves forward into the wind, it operates in a 'windmill state where it extracts energy from the wind. The same is expected if it moves backwards slowly. However, when the turbine pitches or surges backwards at a velocity similar to the wake it produces, the tip and root vortices can recirculate around the rotor resulting in flow detachment and a reduction in lift. This is called 'vortex-ring state' (VRS) [2, 6, 14], a transitional flow condition first described with respect to helicopters in vertical descent [22]. As the wind turbine continues and reaches it's downwind apex, the rotor cannot adjust to the sudden change in relative velocity quickly enough due to its own inertia and begins to inject energy into the flow field like a propeller; hence the term 'propeller state'. Under such a scenario, the thrust will be negative whilst for windmill state it will be positive. Modelling of this flow cycle cannot be done with the use of blade element momentum (BEM) theory as it violates the momentum balance assumption [6]. Therefore, more comprehensive solvers which capture the full aerodynamics must be adopted if propeller state is to be studied.

Few have studied when VRS or propeller state will occur, or the impact it may have on rotor performance. Sebastian & Lackner [6] identified that VRS arises most when the turbine is experiencing below-rated wind speeds, with a higher occurrence rate with increasing radial position. Later they found that propeller state happens most frequently at the root but that the tip region can also experience propeller state at above rated wind speeds [14]. They attributed the onset of propeller state to influences by the root and tip vortices. As one of the first studies to look at this phenomenon in isolation, Leble & Barakos [23] investigated the occurrence of VRS for a 10 MW wind turbine using CFD with prescribed pitching. They identified

the onset of VRS by assessing the induced velocity ratio, where negative signified normal state, between -1 and 0 exhibiting VRS and positive values showed propeller state; the sign convention was switched to match that of rotorcraft. Whilst they identified the onset of VRS, they did not witness any sign of propeller state.

As of now, there appears to be a need for further studies investigating propeller and vortex ring state occurrence for floating offshore wind turbines. Therefore, the aim of this work is to investigate in more detail the causes of propeller and vortex ring state. An idealised situation will be reporduced in which propeller state and vortex ring state are likely, and the underpinning cause of each will be explored. In an attempt to isolate the propeller and vortex ring state onset, complicating factors will be eliminated where possible, namely wind shear, wave effects and rotational platform motion. The focus here is on 1D translational platform motion only, that is expected to produce propeller state: surge. As it often stands out as the DoF with the most significant response, as well as being the motion that first highlighted the phenomenon for helicopters in vertical descent [22], it is the clear starting point for exploring propeller state in more detail. Actuator disc theory will be used to estimate under which wind and surge conditions propeller state might occur. This is then used as a guide to specify the conditions to be simulated using CFD.

The wind turbine used for the present study is introduced in §2 and its main properties shown. An analysis of the surge motion expected using a barge-type platform at a high sea state is then carried out in §3. The computational set-up to recreate the desired surge motion is then described in §4 with the mesh validation study shown in §5. Finally, the results from the analysis are presented and the cause for propeller state and vortex ring state discussed in §6.

2. The NREL 5 MW turbine

Jonkman et al. [8] developed the NREL 5MW reference wind turbine in order to standardise research within the field of wind energy, particularity offshore. This turbine represents a utility-scale wind turbine with aerodynamic, structural and operational data all made fully available in their documentation. All aerofoil data provided, including aerofoil profiles [24], blade twist and chord lengths at 17 span locations, allow for a full 3D model to be recreated (see Fig. 2). The main properties of the turbine are shown in Tab. 1.

3. Platform surge motion

The platform motion response to be expected using the 5MW baseline turbine on a tension-leg platform and barge was studied by Wayman et al. [25] who combined the FAST software package with wave loading and response software

Table 1: Properties of the NREL 5MW reference wind turbine by Jonkman et al. [8].

Turbine parameter	Value	Unit
Rated electrical power	5	MW
Rotor orientation	Upwind	-
Rotor configuration	3 blade	-
Rotor diameter	126	m
Hub diameter/height	3/90	m
Cut-in/rated/cut-out speed	3/11.4/25	ms⁻¹
Cut-in/rated rotation rate	6.9/12.1	rpm
Rated tip speed	80	ms⁻¹
Shaft tilt/pre-cone	5/2.5	degrees

WAMIT. In their study, they assessed the response amplitude operators (RAO) for each of the platforms by changing the wind speed and sea depths. The RAO can be used to predict the surge of the whole system at a given sea sate, where the translational RAO is defined as:

$$RAO_i(\omega) = \left| \frac{\Xi_i(\omega)}{A_{wave}} \right| \qquad i = 1, 2, 3 \qquad (1)$$

where ω is the wave frequency, Ξ is the system response amplitude and A_{wave} is the wave amplitude. Here, $i = 1, 2, 3$ represents surge, heave and sway, respectively. Eq. 1 is therefore used to determine the surge amplitude of the system at any given wave amplitude.

The barge platform responds at a higher wave frequency than the tension-leg platform whilst the tension-leg plaform responds very strongly in surge at lower wave frequencies (approximately 0.1-0.25 rad/s) [25]. The barge surge response spectrum remained relatively constant above water depths of 30 m and was unchanged across all wind speeds tested between 9-25 m/s [25]. It is therefore assumed that the barge surge response can be represented as a function of the sea state, but independent of wind speed. In the results by Wayman et al. [25] the barge surge RAO peaked at a value of 5 when subjected to a wave period of approximately 8.1 s.

To select a wave condition that is both likely to result in propeller and vortex ring state, and is also possible in reality, sea conditions at 40 different UK sites over a period of 7 years were studied from the Fugro GEOS archive [26]. The archive holds data on counts of significant wave height, H_{sig}, and wave periods during this time frame. The wave period probability, and probability of each significant wave height during a wave period of 8-9 s, is shown in Figure 3 and 4, respectively. Consdiering the wave period of 8-9 s from the Fugro archive, when the surge RAO will be approximately 5, some of the highest significant wave heights recorded were in the region of 5-5.5 m . Although infrequent, they are likely to occur several times over the life of a wind farm.

A wave amplitude, A_{wave}, of 1.87 m is used in the present study that coincides with the significant wave height region above following the expression given in [27]:

$$A_{wave}^2 = \frac{H_{sig}^2}{8} \qquad (2)$$

With the surge RAO of 5 as described by Wayman et al. [25], the surge amplitude, A_s, would be 9.4 m. The combination of platform surge and frequency to be simulated here was therefore 9.4 m at a period of 8.1 s.

Further analysis of these conditions can predict if propeller state is likely to occur and at which free wind speed, assuming the surge conditions to be independent of wind speed [25]. Considering the surge to be sinusoidal in nature, the surge displacement, x_s, at any point during the surge cycle is given by:
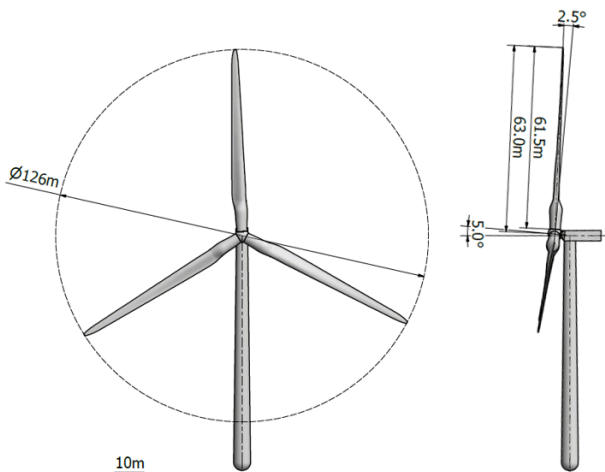

Figure 2: Recreated NREL 5MW turbine model from the data provided in [8, 24]. The main dimensions are shown, including the blade length of 61.5m, rotor diameter of 126m, shaft tilt of 5° and pre-cone of 2.5°.
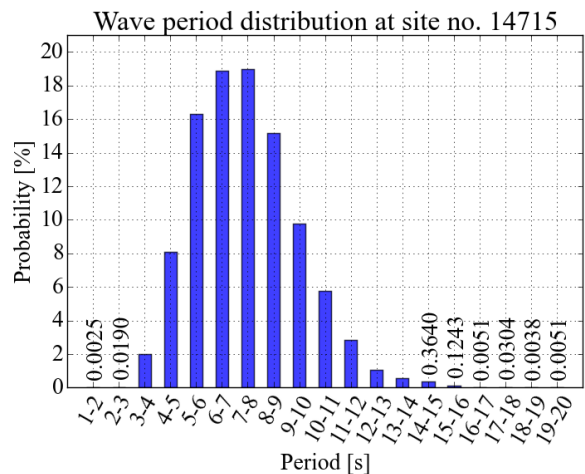

Figure 3: Wave period distribution for the Northern North Sea, site 14715, from the Fugro GEOS archive [26].

3

$$x_s = A_s \sin(\omega_s t) \tag{3}$$

where A_s is the surge amplitude in metres, ω_s is the surge frequency in rad/s and t is time in seconds. The surge velocity is given by:

$$u_s = \frac{dx_s}{dt} = A_s \omega_s \cos(\omega_s t) \tag{4}$$

with the maximum surge velocity:

$$u_{s,max} = A_s \omega_s \tag{5}$$

For propeller state to occur, the thrust of the rotor will be acting against the free wind direction. This could be seen with a negative thrust coefficient, considering windmill state is the regular operating conditions. Therefore, should the flow velocity at the rotor, u_r, be less than the surge velocity, u_s, at any point during the surge cycle, i.e. $u_r < u_s$, it is possible that the rotor is experiencing propeller state. Under these conditions, VRS could also become apparent as the root and tip vortices cannot be propagated downstream and so have the potential to recirculate within the rotor plane as the rotor rotates.

The flow at the rotor is based on the axial induction factor, a, which is defined based on the actuator disc (AD) theory as:

$$a = \frac{u_\infty - u_r}{u_\infty} \tag{6}$$

where u_∞ is the free-stream velocity. By applying AD theory, the result for the coefficient of power is given by:
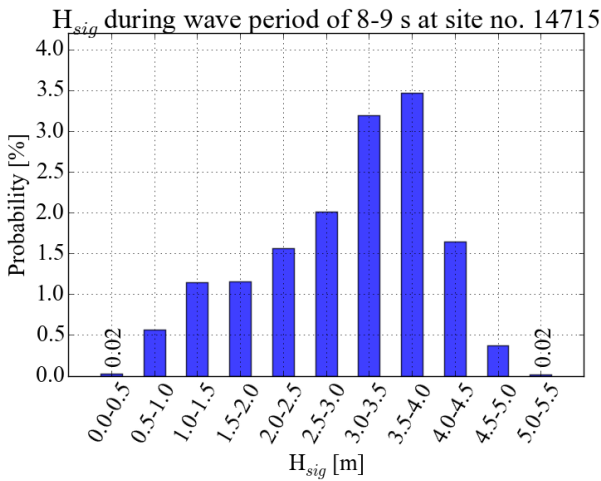
$$C_P = 4a(1-a)^2 \tag{7}$$

Figure 4: Significant wave height distribution, H_{sig}, during a wave period of 8-9 s for site 14715 of the Fugro GEOS archive [26].

Table 2: Wake velocity just behind the NREL 5 MW turbine at wind speeds between cut-in and rated wind speed. Surge velocity is taken here as the max surge velocity of 7.27 m/s from Eq. 5. Text highlighted in red indicates that propeller state is likely to occur at that free wind speed and sea state.

u_∞ [m/s]	a [-]	u_r [m/s]	$u_r - u_{s,max}$ [m/s]
11.4	0.1697	9.47	2.20
11.0	0.1744	9.08	1.81
10.0	0.1762	8.24	0.97
9.0	0.1768	7.41	0.14
8.0	0.1773	6.58	**-0.69**
7.0	0.1773	5.76	**-1.51**
6.0	0.1732	4.96	**-2.31**
5.0	0.1580	4.21	**-3.06**
4.0	0.1258	3.50	**-3.77**
3.0	0.0587	2.82	**-4.45**

which is used to calculate the axial induction factor, leading to the velocity of the flow at the rotor being determined by rearranging Eq. 6 to provide:

$$u_r = (1-a)u_\infty \tag{8}$$

If the flow velocity at the rotor minus the surge velocity is below zero at any point during the surge cycle, propeller state or VRS could occur. To first order, assuming a constant axial induction factor and not including any higher order effects (e.g, tip losses or rotational augmentation), this is observed when:

$$\left[(1-a)u_\infty - A_s \omega_s \cos(\omega_s t)\right] < 0 \tag{9}$$

Tab. 2 therefore suggests that VRS or propeller state could occur, not considering any external influences such as 3D effects, if the free wind speed is 8 m/s or below for a surge amplitude of 9.4 m and a wave period of 8.1 s. Text highlighted in red indicates that the velocity at the rotor is less than the maximum surge velocity and so has the potential to experience VRS or propeller state. To ensure an onset is possible, yet maintaining conditions with a significant energy yield, a free wind speed of 7 m/s was chosen for the simulations.

Plotting the left hand side of Eq. 9 against time with a free wind speed of 7 m/s served as an initial estimation of when either state could initiate and for how long. The simulation was run for 3.8 s under fixed-base conditions to establish the flow, followed by 2 surge cycles at 8.1 s each bringing the total simulation time to 20 s. This plot of relative velocity is shown in Fig. 5, with the rated wind speed of 11.4 m/s also compared in this plot. Based on this, it is clear that with a free wind speed of 7 m/s and the current surge conditions, the rotor will experience a relative rotor velocity of less than zero during the surge cycle for approximately 2 s. With the rated wind speed

Table 3: The rotor rotation rate, free wind speeds, surge amplitudes and surge frequencies of the 4 simulations run. Each simulation has been given a label.

Label	Rotation rate [rpm]	u_∞ [m/s]	A_s [m]	Surge period [s]
RF	12.10	11.4	-	-
RS	12.10	11.4	9.4	8.1
BF	8.47	7.0	-	-
BS	8.47	7.0	9.4	8.1

however, this should not happen. Both 7 m/s and 11.4 m/s were therefore used as the free wind speeds to be investigated. It is worth mentioning that the maximum wave amplitude seen during the 7 year period by Fugro [26] will be above the value of A_{wave} used here. As so, the wave amplitude could be higher and the free wind speed at which the turbine will experience a negative relative velocity will lower, ceteris paribus.

Simulating two wind speeds, both with and without surge, gave four sets of results as shown in Tab. 3. To avoid repetition, each simulation was given a label: RF, RS, BF and BS, respectively, where the R stands for 'Rated' wind speed, the B stands for 'Below' rated wind speed, F stands for 'Fixed' and S stands for 'Surge'. As an example, 'RF' refers to the simulation run at Rated wind speed under Fixed base conditions.

4. Computational methodology

The work in this paper has been carried out using OpenFOAM v1712 [28]. This software uses the finite volume method, solving the incompressible Reynold's Averaged Navier-Stokes (RANS) equations which consists of the mass and momentum conservation equations, respectively [29]:
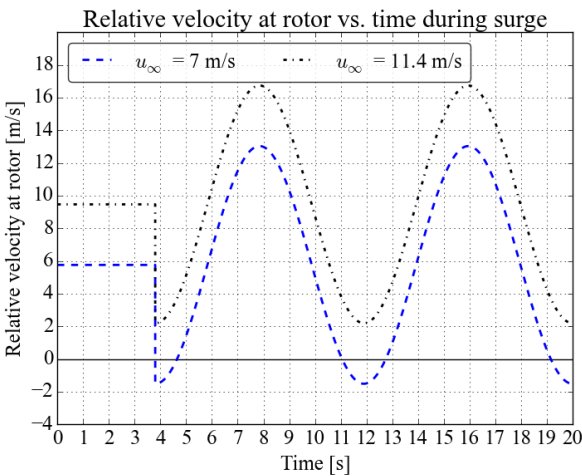

Figure 5: Relative velocity at the rotor using a free wind speed of 7 m/s and 11.4 m/s, surge amplitude of 9.4 m and period of 8.1 s.

$$\frac{\partial \bar{u}_i}{\partial x_i} = 0 \tag{10}$$

$$\frac{\partial \bar{u}_i}{\partial t} + \frac{\partial}{\partial x_j}(\bar{u}_j \bar{u}_i) = -\frac{1}{\rho}\frac{\partial \bar{p}}{\partial x_i} + \frac{\partial}{\partial x_j}\left[2\nu \bar{s}_{ij} - \overline{u'_j u'_i}\right] \tag{11}$$

where $-\overline{u'_j u'_i}$ is the Reynolds' stress tensor and $\bar{s}_{ij}$ the mean strain rate tensor given by:

$$\bar{s}_{ij} = \frac{1}{2}\left(\frac{\partial \bar{u}_i}{\partial x_j} + \frac{\partial \bar{u}_j}{\partial x_i}\right) \tag{12}$$

The Reynolds' stress tensor, $-\overline{u'_j u'_i}$, produces 6 additional unknowns and must be approximated using a turbulence model during the solution process [30]. This is done using the Boussinesq eddy-viscosity approximation which takes the Reynolds' stress tensor and models it as:

$$\overline{u'_j u'_i} = \nu_T \frac{d\bar{u}}{dy} \tag{13}$$

where ν_T is the turbulent viscosity, or eddy viscosity.

A turbulence model must be selected in order to approximate the eddy viscosity and thereby 'close' the RANS equations. The present simulations were solved using the k-ω SST turbulence model which behaves as a k-ω model in the near wall region and as a k-ϵ model in the outer boundary layer. This is done by transforming the k-ϵ model into a formulation of the k-ω model in the free stream and outer boundary layer [20, 31]. This takes advantage of where each individual model performs best and combines them into one model, suitable for handling strong adverse pressure gradients such as that seen by a wind turbine's blade during operation. The model has been applied successfully by many researchers in the field of wind energy, some of whom studied floating offshore turbines, with promising results [15, 17, 18, 32, 33, 34]. In order to close the RANS equations with an eddy viscosity, two additional transport equations are introduced and solved during the process. These are the turbulent kinetic energy, k:

$$\frac{\partial \rho k}{\partial t} + \frac{\partial \rho \bar{u}_j k}{\partial x_j} = P_k - \beta^* \rho \omega k + \frac{\partial}{\partial x_j}\left[(\mu + \sigma_k \mu_t)\frac{\partial k}{\partial x_j}\right] \tag{14}$$

and specific dissipation rate, ω:

$$\begin{aligned}\frac{\partial \rho \omega}{\partial t} + \frac{\partial \rho \bar{u}_j \omega}{\partial x_j} &= \gamma P_\omega - \beta \rho \omega^2 \\ &+ 2\rho(1 - F_1)\sigma_{\omega 2}\frac{1}{\omega}\frac{\partial k}{\partial x_j}\frac{\partial \omega}{\partial x_j} + \frac{\partial}{\partial x_j}\left[(\mu + \sigma_\omega \mu_t)\frac{\partial \omega}{\partial x_j}\right]\end{aligned} \tag{15}$$

where the production of turbulent kinetic energy, P_k, is:

$$P_k = \mu_t \frac{\partial \bar{u}_i}{\partial x_j}\left(\frac{\partial \bar{u}_i}{\partial x_j} + \frac{\partial \bar{u}_j}{\partial x_i}\right) - \frac{2}{3}\rho k \delta_{ij}\partial \bar{u}_i \partial x_j \tag{16}$$

5

and P_ω is:

$$P_\omega = \rho \frac{\partial \bar{u}_i}{\partial x_j} \left(\frac{\partial \bar{u}_i}{\partial x_j} + \frac{\partial \bar{u}_j}{\partial x_i} \right) - \frac{2}{3} \rho \omega \delta_{ij} \partial \bar{u}_i \partial x_j \qquad (17)$$

Both the turbulent kinetic energy and specific dissipation rate then come together to form the eddy viscosity given as:

$$\nu_T = \frac{a_1 k}{\max(a_1 \omega; \Omega F_2)} \qquad (18)$$

where a_1 is a constant of 0.3, Ω is the absolute value of vorticity and F_2 is:

$$F_2 = \tanh(arg_2^2) \qquad (19)$$

and:

$$arg_2 = \max(2 \frac{\sqrt{k}}{0.09 \omega y}; \frac{400 \nu}{y^2 \omega}) \qquad (20)$$

The turbulence intensity has been taken as 6%, based on the typical values seen at the Horns Rev wind farm [35]. Wind shear has been neglected for the purpose of this investigation.

4.1. Dynamic mesh handling

The platform motion was prescribed in OpenFOAM using the "tabulated6DoF" dynamic mesh option. Using this, the absolute translational and rotational displacement in metres and degrees, respectively, was specified at every time step. The prescribed surge displacement and the resulting velocity is shown in Fig. 6. The entire domain has been rotated by 5° as shown in Fig. 7 to reflect the shaft tilt and prescribe rotation only around the x-axis. In doing so, complications with applying 2-axis rotation were eliminated.

4.1.1. Overset mesh method

The overset mesh method, also known as the chimera method, was first introduced in 1981 by Atta [36]. With this method, individual sub-meshes (such as the wind turbine rotor, tower and background domain) are all created separately and merged into one, where the boundaries between each individual sub-mesh overlap to act as a bridge between the various sub-domains. The regions acting as a bridge are more commonly referred to as "fringe" cells across which the velocity is interpolated. Should cells within the geometries fall entirely within a solid boundary (such as those within the rotor or tower), these cells are ignored rather than solved, being referred to as "hole" cells.

The method has been tested in studies previously for wind turbine simulations, namely by Zahle et al. [33] and Li et al. [32]. Both studies compared the results of the overset mesh method against experimental data and found very good agreement. The method was also been successfully applied by Tran & Kim [17] for floating offshore wind turbine computations.

In the present study, two overset regions have been designated: one for the rotor and one for the tower, as shown in Fig. 8. For each region, a 6DoF file has been assigned to prescribe the movement of that specific region with the "tabulated6DoF" dynamic mesh option. Whilst the tower overset region only surges parallel to the ground, the rotor's region both rotates about the x axis and surges equally with the tower.

4.2. Solver selection

OpenFOAM's overPimpleDyMFoam solver allows for the overset mesh technique to be used for a transient simulation. This solver utilises the PIMPLE algorithm, the merged PISO-SIMPLE algorithm, which first runs loops of steady state iterations (SIMPLE) at a given time step until convergence before moving on in time (PISO) [37]. In doing so, the Courant Number can be greater than 1 so
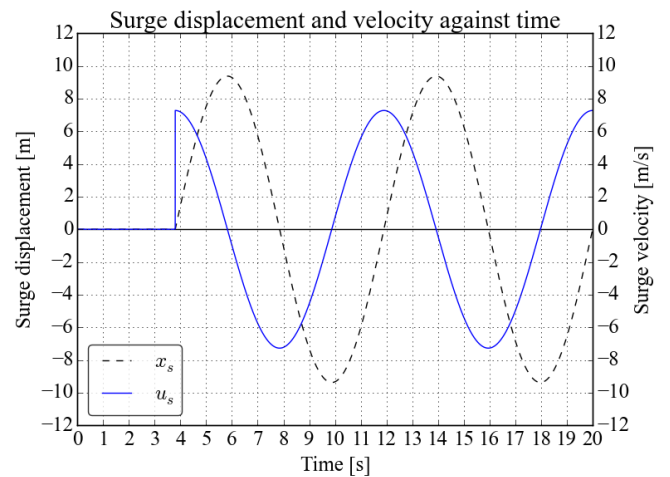

Figure 6: Surge displacement, x_s, and velocity, u_s, with surge amplitude of 9.4 m and period of 8.1 s after a delay of 3.8 s with no surge motion active.

Figure 7: The entire domain has been rotated by 5°, reflective of the shaft tilt, in order to produce a single-axis rotation about the rotor's centre of rotation. All boundary and initial conditions are adjusted accordingly to maintain flow parallel to the ground.

that simulations can be accelerated, whereas for a PISO-only algorithm it must remain below 1 to ensure stability. In the current simulations, the Courant Number has been locked at a maximum of 8 using OpenFOAM's time-step control but averages below 1 for the majority of the blade. The tip region on average is between 1-2. For each time step within the SIMPLE loop the residuals were set to 1×10^{-5} and for every transient time step they were set to 1×10^{-6}, ensuring the case is tightly converged. A maximum of 100 outer corrector loops are run in steady state for each time step before moving on in time, where 2 inner pressure correction loops are run for each of the steady state loops.

5. Mesh generation and validation

OpenFOAM's internal meshing code has been used for all meshing requirements, where blockMesh was used to create the initial background domain (dimensions 600 m × 300 m × 300 m) and snappyHexMesh to mesh the turbine and refinement regions.

The immediate region downwind of the tips and nacelle have been given a higher level of refinement in order to capture the tip and root vortices as they progress downstream. From the hub centre, the fine level of refinement in the immediate near wake extends 30 m (approximately 1/2 rotor radius) downstream at high refinement and to 55 m (approximately 90% rotor radius) at medium refinement as shown in Fig. 9 & 10. As the rotor will surge upwind by 9.4 m, the fine level of refinement upwind extends 15 m to ensure the rotor does not translate out of this zone during its surge cycle.
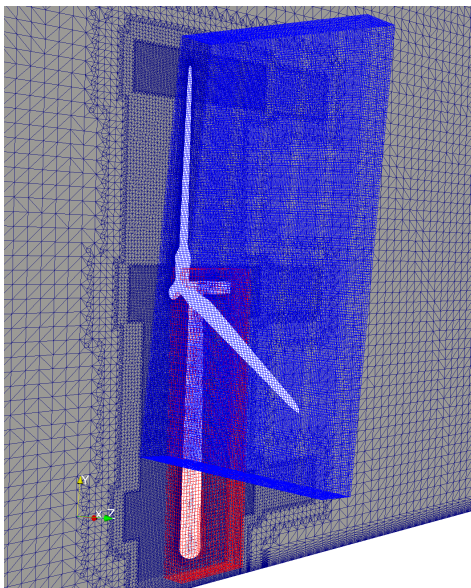
Ten mesh layers are defined on the sea surface, for a

Figure 8: The rotor and tower are enclosed within their separate overset regions and move independent of the background mesh. The rotor's overset region is shown in blue whilst the tower's is in red.

total thickness of 6 m, with a surface roughness value of 0.001 m to reflect that of rough open sea [38] whereas the remaining domain walls have been given a "slip" velocity boundary condition. The rotor and tower have been assigned a "moving wall velocity" boundary condition as they will have motion prescribed onto them. The inlet velocity has been given an "fixed value" condition and the outlet has been given a "inlet outlet" condition to ensure conservation can be held. As for pressure boundary conditions, the walls, rotor, tower and inlet are set to zero-gradient and the outlet is a "fixed value" specified as the internal field. All overset boundaries have been given the "overset" type boundary conditions.

5.1. Grid independence test

Five mesh cases were created starting with a coarse mesh of 4.40 million cells. The number of blockMesh cells was then increased by 10-15%, in turn creating a more detailed mesh during the snappyHexMesh process, with the finest mesh having 11.13 million cells. Each case was run for up to 3 seconds at rated wind speed to assess how the calculated thrust coefficient would compare between the mesh refinement levels. Once an increase in cell count would not change the calculated thrust coefficient, the mesh can be considered converged. The final results of this study are shown in Figure 11, where it is clear that
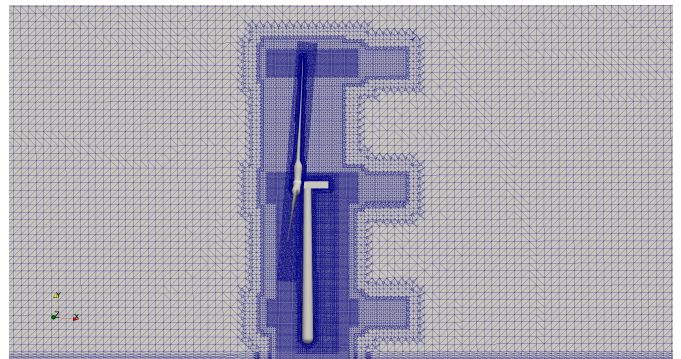

Figure 9: Cut of the background mesh showing where most cells have been located, namely in the near wake and tip/root vortex production area.
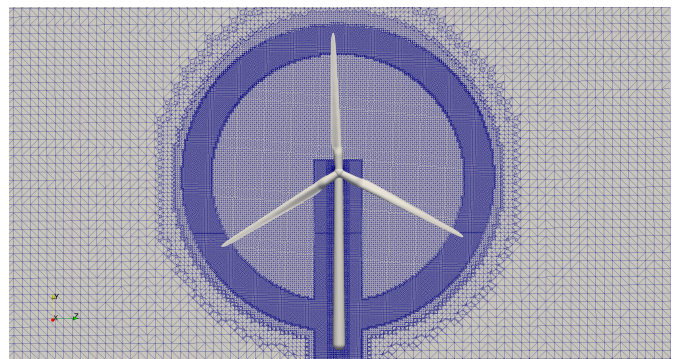

Figure 10: Cut of the cylinder to capture the tip vortices, having a thickness of 13 m.

4.40 and 5.60 million cells were not sufficient however 8.38, 9.71 and 11.13 million cells are showing convergence. With 9.71 and 11.13 million cells in particular producing similar results, it is clear that approximately 10 million cells and above can be considered well converged. As so, the 10.71 million cell case was taken forward .

A second grid independence test was done by continuing both the 9.71 and 11.13 million cell cases into the first surge cycle. The results of this test are shown in Figure 12. There appears to be flow separation between 6.0 and 7.5 s and so a difference is expected considering wall modelling has been employed, however attached flow between the two cell cases matches very well. Except for instances of flow separation, the mesh resolution with 9.71 million cells appears to be sufficient to reproduce converged flow. Since the focus of this study, namely propeller state, does not involved separated flow, this mesh was deemed appropriate and chosen for the simulations presented here.

5.2. Wall model validation

The k-ω SST turbulence model was selected using a wall model to avoid solving all the way to the blade walls which is very computationally demanding, particularly at high Reynolds numbers. Four layers were applied to the rotor patches that are a total of 25 mm thick at the tip region and 30 mm elsewhere to ensure that first cell in the boundary layer is within the log layer [30]. The expansion ratio used is 1.2, where the cell centre of the layer closest to the wall is 2.3 mm normal to the wall. A slice of the mesh at the tip region showing the layer mesh is given in Fig. 14. The y^+ values on the rotor and tower for the BF and RF cases can be seen in Fig. 13 where for the rated wind speed case the y^+ value does not exceed 600 and for the below rated wind speed it does not exceed 400.

To confirm that this wall resolution is sufficient to capture the boundary layer, a small side-study compared lift and drag coefficients of a 2D profile at 95% blade span at various y^+ values. Rated wind speeds at that span location were applied using mesh settings reflective of the full 3D case with 4 layers. Steady state was assumed and solved using the simpleFoam solver. From the results shown in Fig. 15, it is clear that the mesh is suitable if the maximum y^+ value remains below approximately 800, above which the accuracy of the coefficients drop significantly. It is therefore concluded that a y^+ value of 600 and below, as is the case here, will reflect a realistic boundary layer.

6. Results and discussion

The Cirrus supercomputer, with 10,080 cores over 280 nodes run by Edinburgh Parallel Computing Centre (EPCC) [39], was used for the work shown here where each simulation was run in parallel with 576 cores. With the PIMPLE algorithm being employed, the Courant number was set to a maximum of 8. The time step considering this Courant number settled at 3.4×10^{-4} s for the rated wind speed cases and 5.0×10^{-4} s for the below rated cases where each time step represents a rotor rotation of 0.025°. Simulations took between 9 and 12 days of continuous computation to complete.

The first half of the first surge cycle will not reflect a realistic initiation of surge. For this reason, to investigate a surge motion which reflects that of a developed surging turbine, the first 9s of the simulation have been excluded from the plots as a settling period since it begins from rest with no ramp up.

The thrust coefficient acting on the rotor as a whole as well as for each blade individually is shown in Fig. 16 and 17 for the RF and RS cases and Fig. 18 and 19 for the BF and BS cases. As was anticipated, the RS case does not experience propeller state at any point during its surge cycle, either for the rotor as a whole or the tip
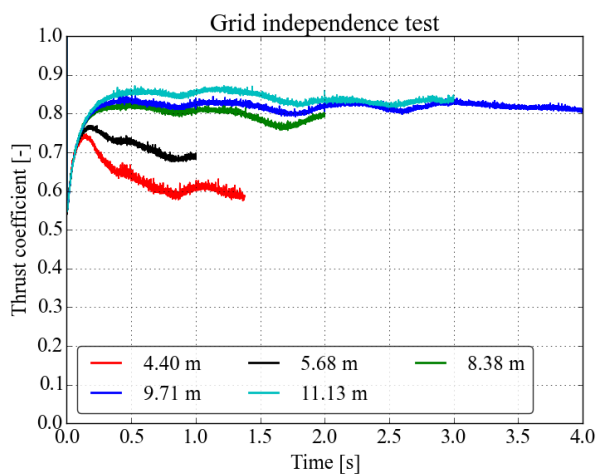

Figure 11: Grid independence study ranging from 4.40 million cells up to 11.13 million, showing particularly good convergence for the 9.71 and 11.13 million cell tests.
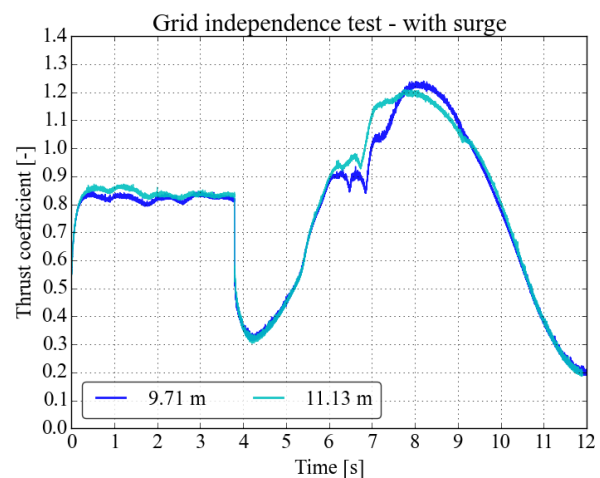

Figure 12: Second grid independence test carried out during the first surge cycle using the 9.71 and 11.13 million cell count cases.
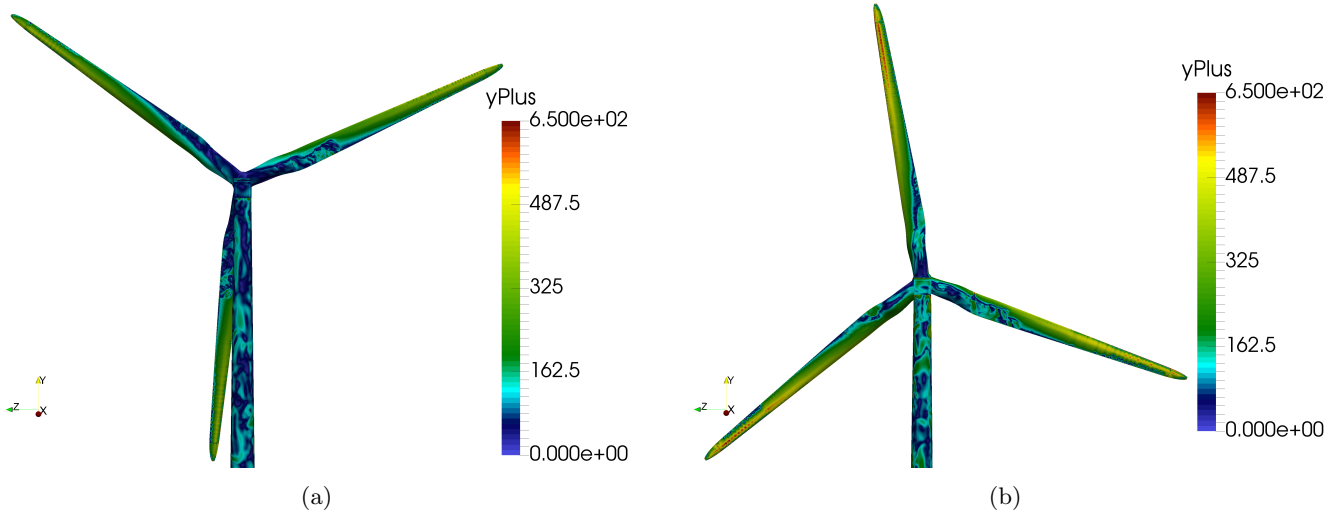
Figure 13: y^+ values over the rear of the rotor, where the air is accelerated the most, for (a) the BF case at 20 s and (b) the RF case at 20 s. The maximum value on the blade in the BF case does not exceed approximately 400 whilst for the RF case it does not exceed 600.
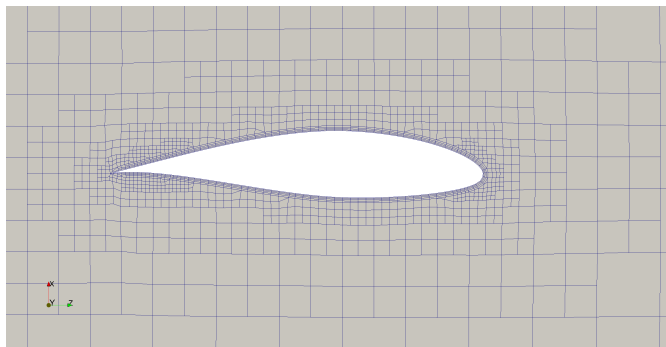

Figure 14: Slice view of the mesh at 90% blade span. 4 layers have been added to the blade patch to capture the boundary layer and ensure the first cell is within the log layer, as required with wall modelling [30].
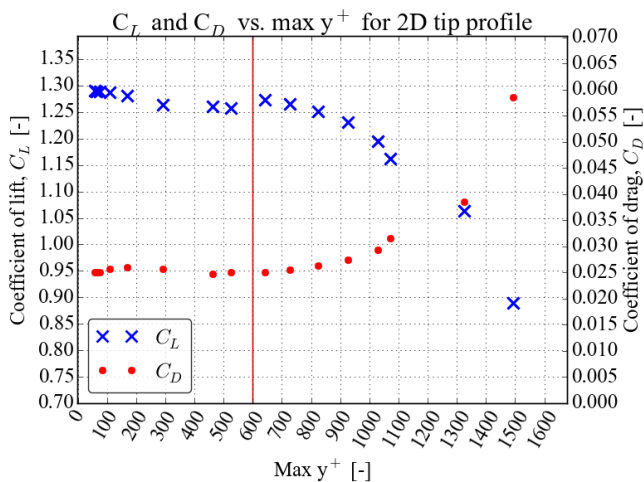

Figure 15: Comparison of steady-state 2D lift and drag coefficients at various y^+ values at 95% blade span and rated wind speed conditions. Red line shows the maximum value across all simulations here.

regions in isolation. Examining the rotor thrust coefficient for the BS case in Fig. 18b however showed that there is clear evidence of propeller state occurrence between 11 s and 13 s where the thrust coefficient temporarily drops below zero. Likewise at 19 s it is seen to commence once more as the surge velocity reaches its maximum. This is in line with what was predicted using actuator disc theory where a negative relative velocity at the rotor could initiate propeller state (Fig. 5).

Although the rotor as a whole temporarily experienced a negative thrust, the tip region did not as shown in Fig. 19b. Velocity magnitude and pressure plots at 1/3 and 90% blade span during propeller state shown in Fig. 20 confirm this finding. The flow around the aerofoil at 1/3 blade span does indeed reflect propeller-like conditions with a low pressure region on the pressure side. At the tip region however, the flow appears to be that of a windmill-operating aerofoil with higher pressure on the pressure side than on the suction side.

The initiation of propeller state and unsteady flow can be explained by looking at the angle of attack at each blade span during these events. For propeller state, at the instant the surge velocity exceeds the flow velocity at the rotor, the only velocity seen at the rotor will be rotational. At this point, the angle of attack becomes the negative of the blade twist. For the unsteady conditions, as the surge velocity increases against the free wind direction, the relative velocity at the rotor plane likewise increases which increases the angle of attack at all blade span locations. Fig. 21 shows the angle of attack acting at each rotor span location under fixed-based conditions, the negative of the blade twist to represent the angle of attack at the instant the relative rotor velocity is zero, i.e. propeller state, and at 16s during the unsteady flow conditions. It also shows the angle of attack at which each blade span location will produce a negative lift coefficient [24], derived from the
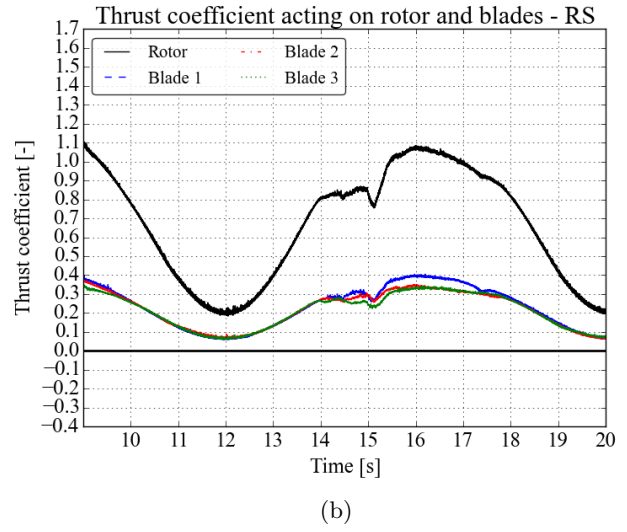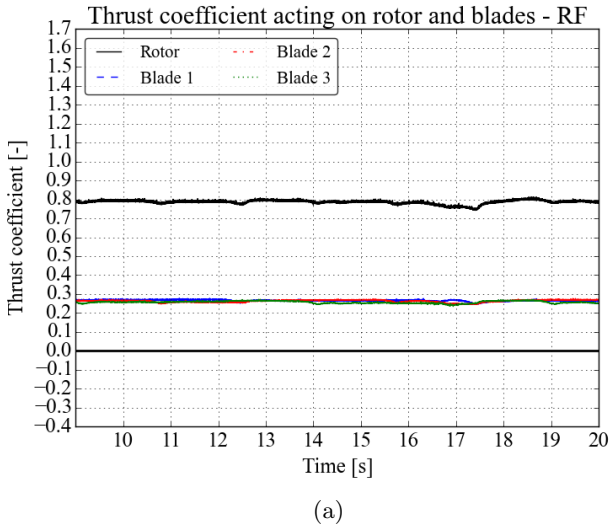
9

Figure 16: Thrust coefficient acting on the rotor as a whole and each blade individually for (a) the RF case and (b) the RS case from 9 s to 20 s.
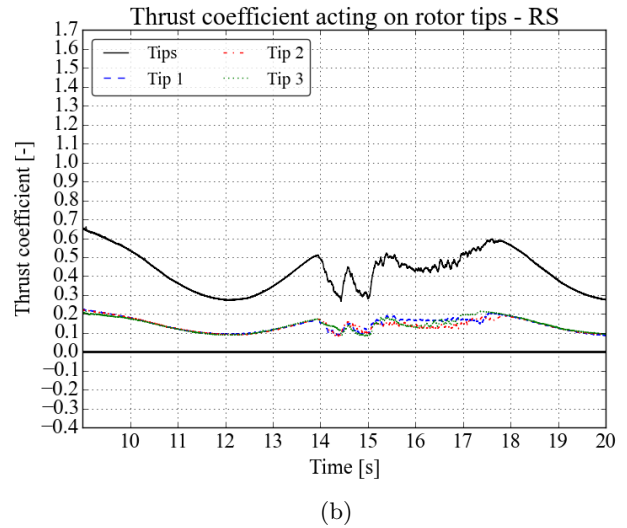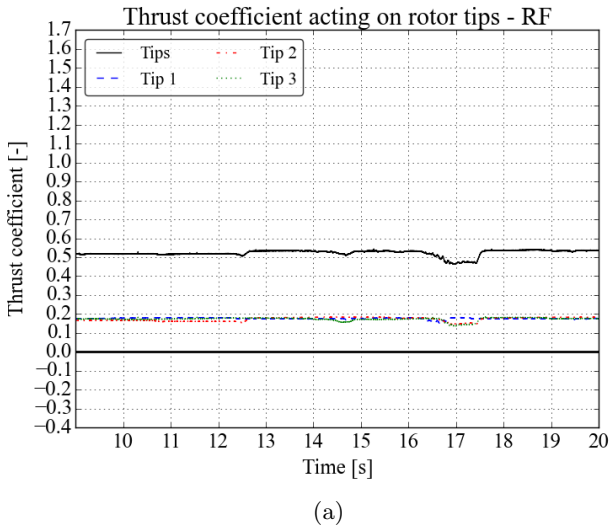

Figure 17: Thrust coefficient acting on the tips as a whole and each blade tip individually for (a) the RF case and (b) the RS case from 9 s to 20 s.

lift to drag ratios of all aerofoils used as shown in Fig. 22 between angles of attack of -40º and 40º. During the propeller state event, the higher blade twist at inboard spans results in a highly negative angle of attack, so much so that the lift coefficient becomes negative to force those spans to behave like a propeller. Although the angle of attack at the tip region also becomes negative, it remains within the positive lift angle of attack region providing a positive tip thrust coefficient at all times, as shown in Fig. 19b, enabling it to remain in windmill state. Should the relative velocity then decrease further below zero, it is clear that spans closer to the tip will also tend towards a negative lift coefficient and propeller state. These findings confirm those of Sebastian & Lackner [14] who found that, at rated wind speeds and below, the root experienced pro-

peller state yet the mid and tip regions did not. Whilst they attributed the onset of propeller state to influences by the root vortex, it would appear in this work to also be connected to a negative angle of attack during a reduction in the relative velocity at the rotor.

What is also clear for both rated and below rated simulations experiencing surge is the indication of heavily unsteady flow as the rotor approaches the maximum surge velocity on its upwind journey. This is shown clearly in the surging thrust coefficient plots with a fluctuation in value between 14 s and 18 s, particularly prominent for the BS case, and shown in Fig. 23 with vorticity isovolumes at 16 s. With NACA 64-618 aerofoils from 71% span and onwards, the angle of attack can increase from 6º at its lowest to over 12º during the unsteady flow. The lift to
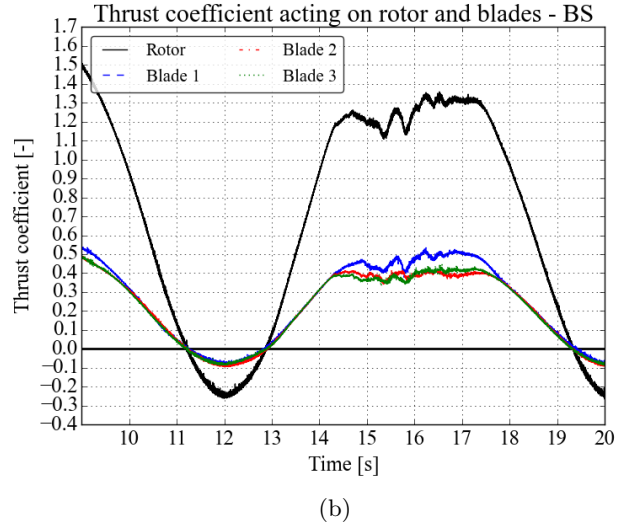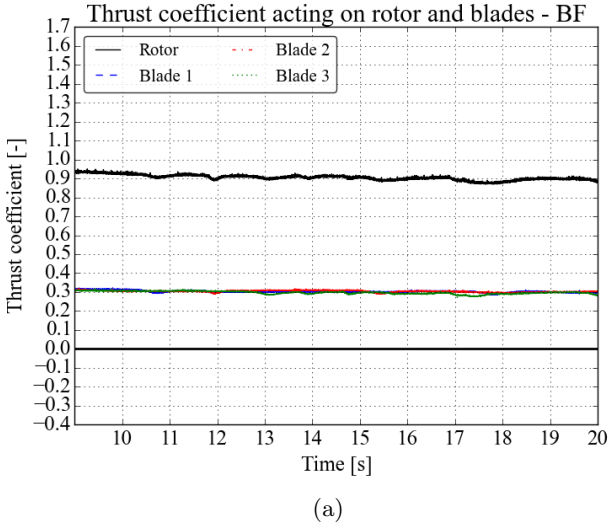
10

Figure 18: Thrust coefficient acting on the rotor as a whole and each blade individually for (a) the BF case and (b) the BS case from 9 s to 20 s.
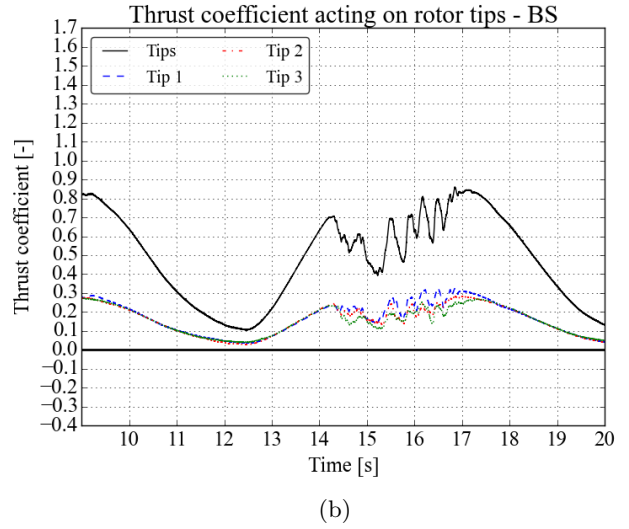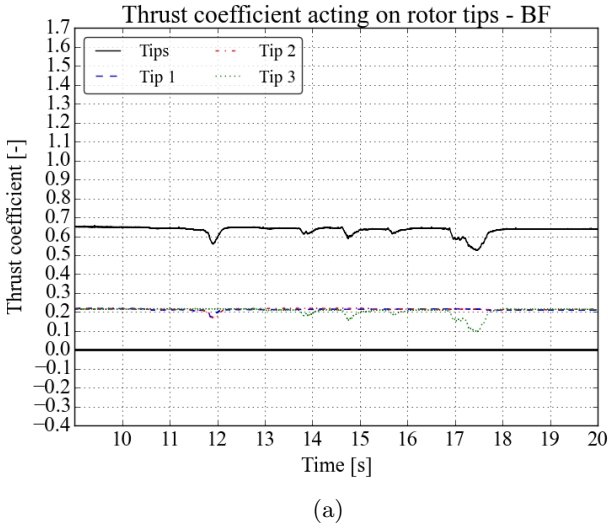

Figure 19: Thrust coefficient acting on the tips as a whole and each blade tip individually for (a) the BF case and (b) the BS case from 9 s to 20 s.

drag ratio for this aerofoil drops rapidly at angles of attack above 10º as shown in Fig. 22, thus the tip region is likely to be experiencing stall at the peak of the upwind cycle. The same can be said for the inboard DU profiles where the angle of attack increases to over 14º and as high as 30º at the root. These profiles will also experience a drop in lift to drag ratio connected with stall at angles of attack greater than 10º. With this in mind, it can be concluded that the root profiles are also susceptible to stalled conditions and flow separation during the rotor's upwind cycle in the absence of active pitch control. Indeed the entire blade span appears to be shedding turbulent flow during stall in Fig. 23. Overall, these findings of stall associated with increasing angles of attack at high surge motions match well with those of Shen et al. [10] and Tran et al. [17].

As a wall model has been used for these simualtions, it is important to note that the boundary layer solution during this flow separation becomes invalid until it reattachment. During such an event, we cannot comment on the causes of propeller state but only highlight that stall is probable. However, the flow does remain attached during propeller state and so the wall model approach is valid at that time.

Whilst propeller state has been clearly identified, so has vortex ring state. The vorticity iso-volumes during the onset of propeller state between 11.5 s and 13 s are shown in Fig. 24. At 11.5 s and 12.0 s, when the mean rotor thrust is negative due to the decrease of inboard angles of attack, there appears to be vortical flow gathering close to the root. At 12.5 s and 13.0 s, there is then a visible event of blade vortex interaction at the tip and strong flow recir-
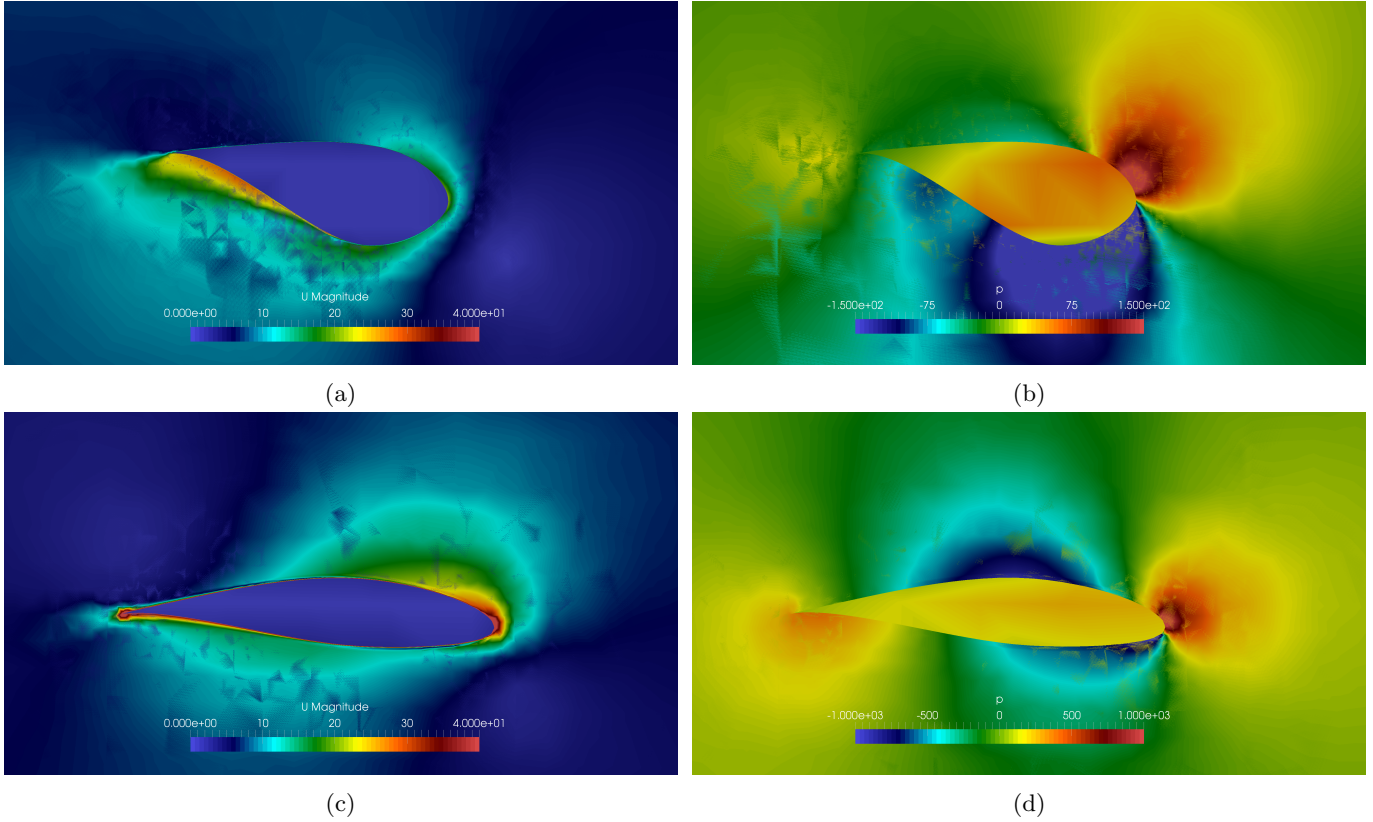
11

Figure 20: Plot of (a) velocity and (b) pressure at 1/3 blade span showing propeller-like conditions, and (c) velocity and (d) pressure at 90% blade span showing normal operating conditions. Plots taken at 12 s during the BS case. The angle of attack for (a) and (b) is approximately -10° and for (c) and (d) is approximately -1°
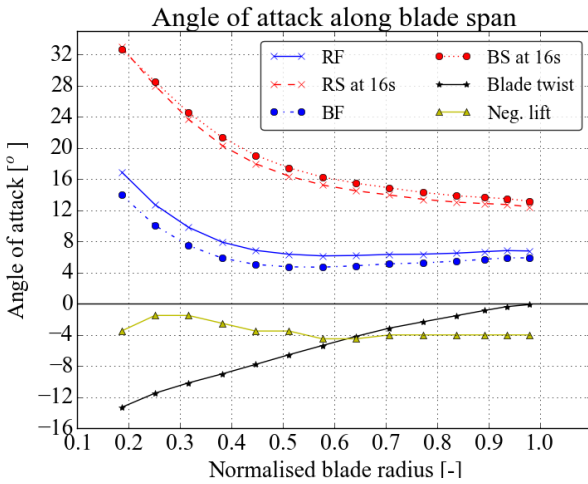
.

Figure 21: Angle of attack acting on the aerofoils of the blade with a fixed base and at 16s with surge active during flow separation. Blade twist is shown as negative to represent the angle of attack of the blade when the relative velocity at the rotor is zero. The 'Neg. lift' plot shows at which angle of attack the respective span location will produce a negative lift coefficient.
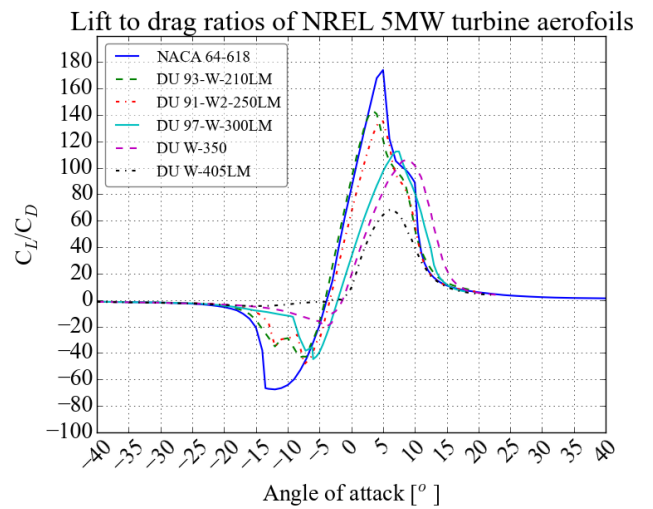

Figure 22: Lift to drag ratios of the aerofoils used in the NREL 5MW wind turbine between angles of attack of -40º and 40º [24].

culation at the root. Based on its definition, this is a sign of vortex ring state. As there is a 2.36 s interval between blade passings when rotating at 8.469 rpm, it is possible that propeller state develops in this time frame prior to a blade striking the tip vortex from the previous blade no more than 2.36 s later. As approximately 2 seconds are
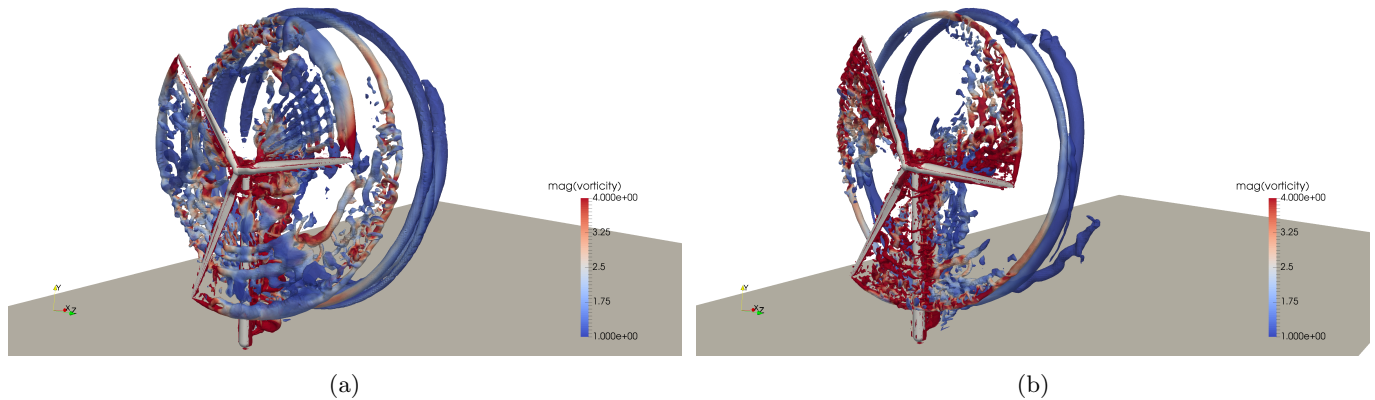
Figure 23: Vorticity isovolume plot at 16 s for (a) the RS case and (b) the BS case when flow separation appears high for both.

spent with a relative rotor velocity that is below zero, it is within this short time frame that the tip and root vortices can no longer be propagated downstream. Although the rotor could recover before a blade interacts with the preceding tip vortex, the thickness of the tip vortex will prevent this as it essentially increases the clearance necessary to avoid all interaction. A negative lift force, or propeller state, is therefore seen as the relative rotor velocity approaches and becomes negative, where it remains negative long enough for a blade tip to pass over the previous tip vortex. The inability to advect the tip and root vortices downstream for a short period of time results in the interaction of the tip vortices and vortex accumulation at the root associated with VRS shortly after.

7. Conclusion

This work has identified and explained the causes of propeller state and vortex ring state using the NREL 5MW rotor when subjected to a surge amplitude of 9.4 m and period of 8.1 s, at a free wind speed of 7 and 11.4 m/s. Whilst the rotor as a whole experienced propeller state at a free wind speed of 7 m/s, the tip region did not as the thrust coefficient remained positive at all times. It was concluded that propeller state is due to a decrease in the angle of attack when the relative velocity at the rotor decreases, so much so that a negative lift coefficient is produced. This is heavily dependant on the blade twist, where spans with a high twist will likely experience propeller state before spans with a lower twist. This explained why the tip region avoided the onset of propeller state as the twist tapers to zero, whilst the rotor as a whole averaged a negative thrust coefficient due to the high twist at mid to root span locations.

Vortex ring state, by definition, was found to occur during the propeller state event, shown by blade vortex interaction at the tips and flow recirculation at the root after the initial onset of propeller state. It is likely that propeller state first develops due to the relative velocity at the rotor decreasing to and surpassing zero, but then

when zero or negative relative velocity is maintained for a duration similar to the blade passing period, the blade tips interact with the vortex from the previous blade as well as an accumulation of root vortices at the hub to initiate VRS.

It is acknowledged that the methodology applied here requires a very high computational resource and can therefore not be developed into a tool to simulate many wind turbines in an array for the many wave and wind conditions experienced by an installation. Instead, it serves to develop a better understanding of the conditions giving rise to propeller and vortex ring states and their effect on turbine performance and blade loadings. This understanding could then be used to develop a parameterisation of these effects within a more practical modelling framework, or to inform the designers or operators of floating wind turbines to implement design or control response to maximise performance while minimising adverse loading.

The immediate future to build up this understanding will extend the simulations over a wider range of wind speeds and surging conditions. Following this, effects of the other turbine motions will be addressed by adding pitching as a further degree of freedom.

References

[1] A. Peiffer, D. Roddier, Floating wind turbines: The new wave in offshore wind power, in: J. H. Lehr, J. Keeley, T. B. Kingery (Eds.), Alternative Energy and Shale Gas Encyclopedia, John Wiley & Sons, Ltd, New Jersey, 2016, pp. 69–79.
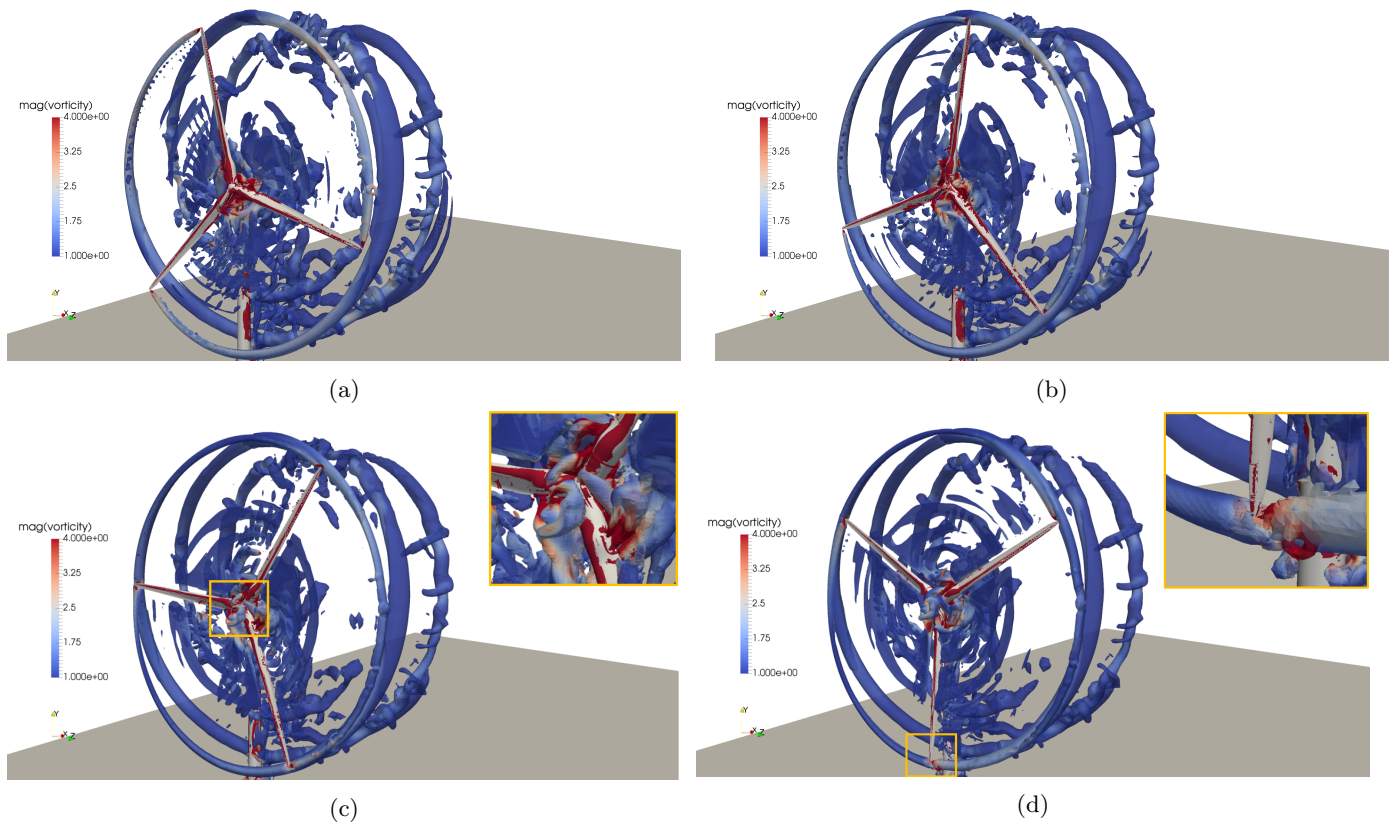
13

Figure 24: Vorticity iso-volumes for the BS case between 11.5 s and 13.0 s during propeller state, with (a) 11.5 s, (b) 12.0 s, (c) 12.5 s and (d) 13.0 s. Blade vortex interaction at the tip as well as flow recirculation at the root is seen to occur in the 12.5 s (c) and 13.0 s (d) snapshots, reflecting vortex ring state conditions.

[2] D. Matha, M. Schlipf, A. Cordle, R. Pereira, J. Jonkman, Challenges in Simulation of Aerodynamics, Hydrodynamics, and Mooring-Line Dynamics of Floating Offshore Wind Turbines, 2011. URL: http://www.osti.gov/bridge.

[3] M. Leimeister, A. Kolios, M. Collu, Critical review of floating support structures for offshore wind farm deployment, Journal of Physics: Conference Series 1104 (2018) 012007.

[4] Carbon Trust, Floating Offshore Wind: Market and Technology Review, 2015. URL: http://www.carbontrust.com/media/670664/floating-offshore-wind-market-technology-review.pdf.

[5] IRENA, Floating Foundations: A Game Changer for Offshore Wind Power, 2016. URL: http://www.irena.org/-/media/Files/IRENA/Agency/Publication/2016/IRENA{_}Offshore{_}Wind{_}Floating{_}Foundations{_}2016.pdf.

[6] T. Sebastian, M. A. Lackner, Offshore Floating Wind Turbines - An Aerodynamic Perspective, in: 49th AIAA Aerospace Sciences Meeting, AIAA, Orlando, Florida, 2011, pp. 1–27.

[7] Principle Power Inc, Principle Power Inc - Home Page, 2015. URL: http://www.principlepowerinc.com/.

[8] J. Jonkman, S. Butterfield, W. Musial, G. Scott, Definition of a 5-MW Reference Wind Turbine for Offshore System Development, 2009.

[9] B. Wen, X. Tian, X. Dong, Z. Peng, W. Zhang, Influences of surge motion on the power and thrust characteristics of an offshore floating wind turbine, Energy 141 (2017) 2054–2068.

[10] X. Shen, J. Chen, P. Hu, X. Zhu, Z. Du, Study of the unsteady aerodynamics of floating wind turbines, Energy 145 (2018) 793–809.

[11] R. Farrugia, T. Sant, D. Micallef, A study on the aerodynamics of a floating wind turbine rotor, Renewable Energy 86 (2016) 770–784.

[12] T. Sebastian, M. A. Lackner, A Comparison of First-Order Aerodynamic Analysis Methods for Floating Wind Turbines, in: 48th AIAA Aerospace Sciences Meeting, Orlando, Florida, 2010, pp. 1–22.

[13] T. Sebastian, M. A. Lackner, Development of a free vortex wake method code for offshore floating wind turbines, Renewable Energy 46 (2012) 269–275.

[14] T. Sebastian, M. A. Lackner, Analysis of the Induction and Wake Evolution of an Offshore Floating Wind Turbine, Energies 5 (2012) 968–1000.

[15] T. Tran, D. Kim, J. Song, Computational Fluid Dynamic Analysis of a Floating Offshore Wind Turbine Experiencing Platform Pitching Motion, Energies 7 (2014) 5011–5026.

[16] T. T. Tran, D.-H. Kim, B. Hieu Nguyen, Aerodynamic Interference Effect of Huge Wind Turbine Blades With Periodic Surge Motions Using Overset Grid-Based Computational Fluid Dynamics Approach, Journal of Solar Energy Engineering 137 (2015) 061003.

[17] T. T. Tran, D.-H. Kim, A CFD study into the influence of unsteady aerodynamic interference on wind turbine surge motion, Renewable Energy 90 (2016) 204–228.

[18] J. Wu, J.-h. Ding, Y.-p. He, Y.-s. Zhao, Study on Unsteady Aerodynamic Performance of Floating Offshore Wind Turbine by CFD Method, in: Proceedings of the Twenty-fifth (2015) International Ocean and Polar Engineering Conference, 2015, pp. 554–560.

[19] Y. Liu, Q. Xiao, A. Incecik, C. Peyrard, D. Wan, Establishing a fully coupled CFD analysis tool for floating offshore wind turbines, Renewable Energy 112 (2017) 280–301.

[20] F. Menter, Improved Two Equation k-w Turbulence Models For Aerodynamic Flows, 1992. URL: http://arc.aiaa.org/doi/

14

        10.2514/6.1993-2906.

[21] D. D. Chandar, H. Gopalan, Comparative Analysis of the Arbitrary Mesh Interface (AMI) and Overset Methods for Dynamic Body Motions in OpenFOAM, in: 46th AIAA Fluid Dynamics Conference, June, American Institute of Aeronautics and Astronautics, Reston, Virginia, 2016.

[22] J. G. Leishman, Principles of Helicopter Aerodynamics, Cambridge University Press, 2000.

[23] V. Leble, G. Barakos, Forced pitch motion of wind turbines, Journal of Physics: Conference Series 753 (2016) 022042.

[24] J. Jonkman, DOWEC-NREL 5MW blade airfoil data-v2, 2012. URL: https://wind.nrel.gov/forum/wind/viewtopic.php?f=2{&}t=440.

[25] E. Wayman, P. Sclavounos, S. Butterfield, J. Jonkman, W. Musial, Coupled Dynamic Modeling of Floating Wind Turbine Systems, in: Offshore Technology Conference, 18287, Offshore Technology Conference, 2006, pp. 1–25.

[26] Fugro GEOS, Wind and Wave Frequency Distributions for Sites around the British Isles, 2001. URL: http://www.hse.gov.uk/researcH/otopdf/2001/oto01030.pdf.

[27] W. T. Sørensen, Renewable energy: its physics, engineering, use, environmental impacts, economy and planning aspects, 3rd ed., Elsevier, 2004.

[28] OpenCFD, OpenFOAM: The Open Source CFD Toolbox User Guide, version v1712, 2018. URL: https://www.openfoam.com/.

[29] J. H. Ferziger, M. Peric, Computational Methods for Fluid Dynamics, 3rd ed., Springer, 2002.

[30] D. C. Wilcox, Turbulence Modeling for CFD, second ed., DCW Industries, 1998.

[31] F. R. Menter, Two-equation eddy-viscosity turbulence models for engineering applications, AIAA Journal 32 (1994) 1598–1605.

[32] Y. Li, K.-J. Paik, T. Xing, P. M. Carrica, Dynamic overset CFD simulations of wind turbine aerodynamics, Renewable Energy 37 (2012) 285–298.

[33] F. Zahle, N. N. Sørensen, J. Johansen, Wind turbine rotor-tower interaction using an incompressible overset grid method, Wind Energy 12 (2009) 594–619.

[34] X. Cai, R. Gu, P. Pan, J. Zhu, Unsteady aerodynamics simulation of a full-scale horizontal axis wind turbine using CFD methodology, Energy Conversion and Management 112 (2016) 146–156.

[35] K. S. Hansen, R. J. Barthelmie, L. E. Jensen, A. Sommer, The impact of turbulence intensity and atmospheric stability on power deficits due to wind turbine wakes at Horns Rev wind farm, Wind Energy 15 (2012) 183–196.

[36] E. Atta, Component-adaptive grid interfacing, in: 19th Aerospace Sciences Meeting, American Institute of Aeronautics and Astronautics, Reston, Virigina, 1981.

[37] T. Holzmann, Mathematics, Numerics, Derivations and OpenFOAM®, 2018.

[38] T. Burton, D. Sharpe, N. Jenkins, E. Bossanyi, Wind Energy Handbook, second ed., John Wiley & Sons, Ltd, 2001.

[39] Edinburgh Parallel Computing Centre (EPCC), Facilities, 2018. URL: https://www.epcc.ed.ac.uk/facilities.